RSC Advances

PAPER

View Article Online
View Journal | View Issue

Cite this: *RSC Adv.*, 2023, **13**, 33736

Study of the electronic effect and quantitative spectra predictions of *o*-methoxyaniline-terminated monoazonaphthols: a combined experimental and DFT study†

Guoxun Zhu,[a] Yan Lin,[b] Wenxian Zhou,[c] Huacan Song[a] and Zhengquan Li*[a]

A combined experimental and density functional theory (DFT) study on the UV-Vis spectra of *o*-methoxyaniline-terminated mono azo dyes was conducted. By applying time-dependent-DFT calculations, details of excitation processes were determined and visualization by hole–electron analysis was undertaken. Fragment-divided analysis revealed the contributions of different parts of the structures for the UV-Vis spectra, that richer/poorer electron density on aromatic rings lead to greater/less maximum absorption wavelengths (λ_{max}) and larger/smaller half peak width ($W_{1/2}$). Combining theoretical prediction with experimental verification, we answered the question of how the electronegativities of substituents affected the electron densities and how it affected the spectra. In addition, a linear model connecting the λ_{max} and $W_{1/2}$ to the chemical shifts obtained by NMR spectroscopy was constructed, which laid the foundation for construction of a spectral library.

Received 14th August 2023
Accepted 13th September 2023

DOI: 10.1039/d3ra05518c

rsc.li/rsc-advances

Introduction

Experimental studies and industrial applications of azo compounds can be dated back to 1863, when Martius and Lightfoot coupled diazonium ions with amines.[1] Since then, azo compounds have been prepared in large varieties and huge amounts owing to the ready availability of raw starting materials, simplicities of experimental control, and varieties of synthetic products. Nowadays, azo dyes are the most applied materials among all types of dyestuffs. They account for >50% of known commercial dyes,[2] including acid dyes, direct dyes, disperse dye, and reactive dyes (Fig. 1).

The hue, saturation, and value of colours are important parameters for controlling the dyeing result, and are closely related to the corresponded UV-absorption spectra. Hence, studies on spectra and designing of dyes have long been the focus of researchers.[3a–c]

The colours of azo dyes are controlled mainly by the numbers of azo bonds, and fine-tuned by the coupled skeleton and substituted groups. Embedding electron-donating groups (EDGs) on the skeleton can red-shift λ_{max} to larger values, whereas electron-withdrawing groups (EWGs) provide the opposite effect. For instance, transforming nitro functional groups to amino functional groups by reduction reactions can red-shift the λ_{max} by ~20 nm.[4a] Wu and coworkers found the λ_{max} of 2,5-dimethyl-4-((4-nitrophenyl)diazenyl)phenol red-shifted from 390 nm to 399 nm after alkylation at the hydroxyl group.[4b] However, a deeper mechanistic study to provide quantitative predictions was hindered by the diversities of azo skeletal structures, and quantitative analysis has rarely been reported.

With the prosperities of delicate applications of dyes such as dye-sensitized solar cells,[5a,b] dye-based OLEDs,[5c] dye-based polarizers,[5d] and dye-doped liquid crystals,[5e,f] meticulous theoretical guidance for the prediction of optical properties, such as λ_{max}, peak width, and absorption intensity, is urgently needed. Conversely, the innovation of time-dependent density-functional theory (TD-DFT)[6a–c] and developments of analytical methods for excited states[7a–d] have supplied possibilities to establish quantitative relationships between the structure and optical properties of dyes.

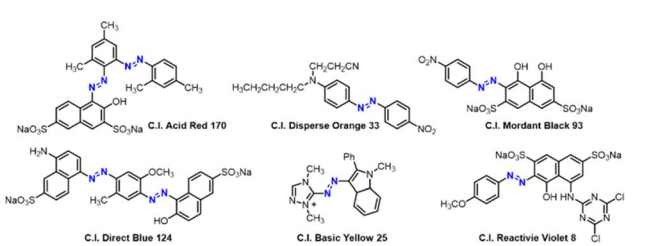

Fig. 1 Some representative azo dyes.

[a]*Guangdong Provincial Key Laboratory of Chemical Measurement and Emergency Test Technology, Institute of Analysis, Guangdong Academy of Sciences, China National Analytical Centre, Guangzhou, 510070, P. R. China. E-mail: 1539888623@qq.com; lzq@fenxi.com.cn*

[b]*FSPG Hi-Tech Co., Ltd, Foshan, 528000, P. R. China*

[c]*WINDA OPTO-Electronics Co., Ltd, Foshan, 528136, P. R. China*

† Electronic supplementary information (ESI) available: Detailed results and coordinates of the optimized species. See DOI: https://doi.org/10.1039/d3ra05518c

In this work, 20 types of mono azo compounds with various substituents embedded on terminated *o*-methoxyaniline were prepared. Spectra were collected qualitatively and quantitatively, alongside theoretical elaborations of the spectra and excited-state analyses. Through a combined experimental–DFT study, details of spectral constitution were confirmed, and a relatively accurate relationship between substituent and spectral parameters was established. This work showed the good combination of a DFT study and experimental research for spectroscopic analyses. Also, qualitative/quantitative conclusions provided accurate guidance for further structural renovations in more complicated applications.

Experimental section

A series of monoazonaphthols were prepared carefully through a diazotization-coupling protocol. Different *o*-methoxyanilines embedded with functional groups of different electronegativity (2,5-dimethoxyaniline (**1**), 2-methoxy-5-methylaniline (**2**), 2-methoxyaniline (**3**), 2-anisidine-4-sulfonic acid (**4**), and 2-methoxy-5-(trifluoromethyl)aniline (**5**)) were diazotized by a reported method[8a,b] with few modifications. The coupling of the diazonium salt with naphthols such as 6-amino-1-hydroxynaphthalene-3-sulfonic acid (**a**), 7-amino-1-hydroxynaphthalene-3-sulfonic acid (**b**), and 2-amino-5-hydroxynaphthalene-1,7-disulfonic acid (**c**) was done in saturated Na_2CO_3 solution with stirring for 2 h. Salted-out treatments were applied in the work-up, and mono azo dyes were obtained by centrifugation. All reactions gave products in moderate-to-good yield with good purities (characteristic data are summarized in ESI†) (Scheme 1).

Next, the prepared azo compounds were dissolved in buffer (pH = 6.86) made with deionized water to obtain dye solutions at 25 ppm. Notably, samples applied in the quantitative test were purified further by dialysis using a semipermeable membrane (100D) to remove salt completely. UV-Vis spectra were collected in quartz cuvettes (path length = *a* 10 mm) taking buffer as the reference. Experimental UV-Vis spectra were obtained after normalization to keep the maximum absorption equal to 1 (unless specified otherwise) (Fig. S1 and S2†).

Computational details

DFT and TD-DFT calculations were carried out using the ORCA 5.0 computational suite[9a–d] applying resolution of identity (RI) approximation (29–30) and tight SCF criteria. Structures were constructed by the Open Babel Program.[9e] Constructed structures were pre-optimized by the MMFF94 force field.[10] Pre-optimized structures were optimized further by the B3LYP functional[11a–c] using the Ahlrichs double-zeta basis set def2-SVP (standard) and def2-SVP/J (auxiliary),[11d] combined with the D3 version of Grimme's dispersion.[11e,f] Frequency analyses were undertaken for optimized structures at the same level and a virtual frequency was not found, which ensured optimization of the structures to a minimum point (more details in ESI†). A CPCM model[11g] was applied to reproduce the solvent environment. Extractions of energies, thermal-correction values, and coordinates were realized by the Shermo program.[9f] Wavefunction analyses, including hole–electron analysis and charge-population analysis, were undertaken by the Multiwfn program.[9g] Analyses of natural bond orbitals were undertaken by the NBO 7.0 program.[9h,i]

Optimized structures were applied for ES study. Excited energies are highly correlated with the Hartree–Fock ratio (HF%) of DFT methods.[12] Therefore, a screening of DFT functionals was done. The pure functional TPSS (HF% = 0)[11h] matched the experimental spectra best (Fig. S5†). Consequently, later analyses of theoretical spectra and ES were all calculated at the TD-TPSS/def2-SVP CPCM (water) level with the def2/J auxiliary basis set and RI approximation. Results calculated at the TD-TPSS/def2-SVP level were applied for wavefunction analyses of excited states.

Results and discussion

Analyses of UV-Vis spectra

With the prepared azo compounds in hand, UV-Vis spectra were collected. The results of λ_{max} are summarized in Table 1. Consistent with literature reports, λ_{max} decreased with the increasing electronegativity of the substituent embedded on *o*-methoxyanilines. Specifically, λ_{max} varied from 509/541/509 nm to 489/526/488 nm for the coupled product of **a**/**b**/**c** (see each row in Table 1). That is, the electron-donating/-withdrawing effect red-shifted/blue-shifted the λ_{max} by 20 nm for mono-azonaphthols. Comparison of the λ_{max} of the coupled product of **a**, **b**, and **c** (see each column in Table 1) revealed that the λ_{max} of **1b–5b** was ~30 nm greater than that of **1a–5a** and **1c–5c**. Usually, different λ_{max} values suggest discrepancies in structural conjugates or differences in the excitation mechanism. Considering the similarity of structures of these mono azo

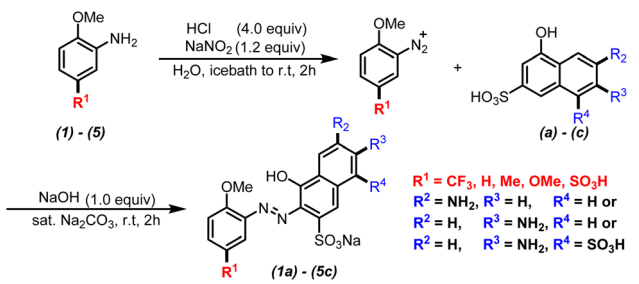

Scheme 1 Synthetic route of azo compounds.

Table 1 Summary of experimental λ_{max} of prepared azo compounds

λ_{max}	Ph[a]				
Naph[b]	1	2	3	4	5
a	509 nm	507 nm	500 nm	492 nm	489 nm
b	541 nm	538 nm	534 nm	529 nm	526 nm
c	509 nm	507 nm	499 nm	491 nm	488 nm

[a] **Ph** represents the types of aniline. [b] **Naph** represents the types of naphthol.

compounds, we believed that differences in spectral absorption were caused mainly by excitation characteristics.

To understand the differences in excitation mechanisms, **3a–c** were selected for case study. As shown in Fig. 2a and c, the peaks of **3a** and **3c** in experimental UV-Vis spectra showed a similar shape. An almost symmetrical peak appeared at 500/499 nm (λ_{max}, Abs. = 1.0) and another weaker absorption signal (Abs. = 0.5) was observed at 304/313 nm. However, **3b** featured different absorption properties, with λ_{max} (Abs. = 0.72) settled at 534 nm with a broad band expanded to over 400 nm, and a peak with similar/greater absorption strength appearing at 303/256 nm (Fig. 1b). The broad absorption band and asymmetrical absorption peak indicated that two or more excitation processes may be involved in formation of the maximum absorption peak of **3b**. Short waves (<400 nm) corresponded to the generation of high-energy ES, suggesting that **3b** preferred to be excited to higher ES.

Theoretical UV-Vis spectra were drawn to test the hypothesis stated above. As shown in Fig. 2b, d, and f, the calculated UV-Vis spectra were generated by overlaying Gaussian-broadening[13] curves of oscillatory strength (**OS**), which reproduced peak shapes and absorption wavelengths qualitatively (more details in ESI†). By referring to these theoretical spectra, three main conclusions could be drawn, as shown below.

(a) The λ_{max} of **3a** consisted of the formation of first singlet ES (**S1**) and second singlet ES (**S2**) from the ground state (**S0**), whose corresponding absorption wavelengths were 529 nm and 461 nm, respectively. The theoretical λ_{max} was shifted to 493 nm after a Gaussian-broadening operation of these two signals by overlaying. The absorption occurring at 304 nm in Fig. 1a was mainly attributed to the formation of high-level **ES** (**S0** → **S8**).

(b) The excitation process changed distinctly in **3b**. The **OS** of **S0** → **S1** was very low, so the λ_{max} of **3b** was mainly supported by **S0** → **S2**. The broad band appearing in the experimental spectra consisted of the formation of numerous and evenly spaced **ES** which had similar **OS**. That is, the absorption curve of **3b** relied on more **ES**, and the strong absorption at short wavelengths (303 and 256 nm in Fig. 1c) was contributed by the overlaying of high-level ES.

(c) For **3c**, the excitation mechanism was similar to that for **3a**. That is, the λ_{max} could be attributed to the excitations of **S0** → **S1** and **S0** → **S3**, whereas the signal appearing at 313 nm was caused by **S0** → **S10**.

Studies on structural–spectral features

To obtain basic understanding of UV-Vis spectra, more in-depth analyses of the relationships between structures and excitation behaviours were carried out. As shown at the top of Fig. 3, the **OS** of the lowest 25 excited singlet states of **3a–c** were visualized by histograms. Consistent with previous inferences, the **OS** in **3b** was distributed over a wider scope at moderate strength (0.15< **OS** < 0.30), which gave the Gaussian-broadening curve of **3b** a broad shape. Relatively, the **OS** in **3a**/**3c** was concentrated and at high strength (**OS** > 0.35), which resulted in narrow and symmetrical absorption signals.

Excitation energy is inversely proportional to the absorption wavelength. As a result, the absorption of λ_{max} was determined by ES being lower than **S6**. Hole–electron analysis was applied to reveal the details of charge transfer among **3a–c** during these excitation procedures. Specifically, a hole (**Hole**) defined the real area where electrons "flow out" whereas an electron (**Ele**) defined where electrons "flow in". As shown at the bottom of Fig. 3, **Hole** and **Ele** mostly located around the azo nitrogen

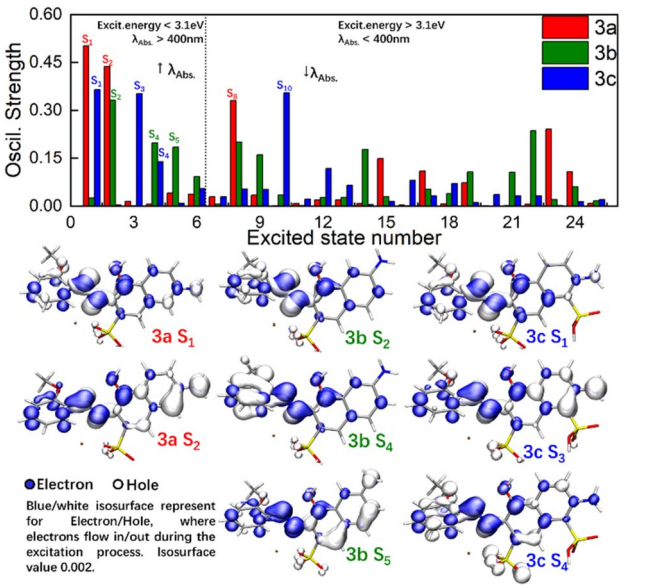

Fig. 3 Visualizations of holes and Ele of 3a–c.

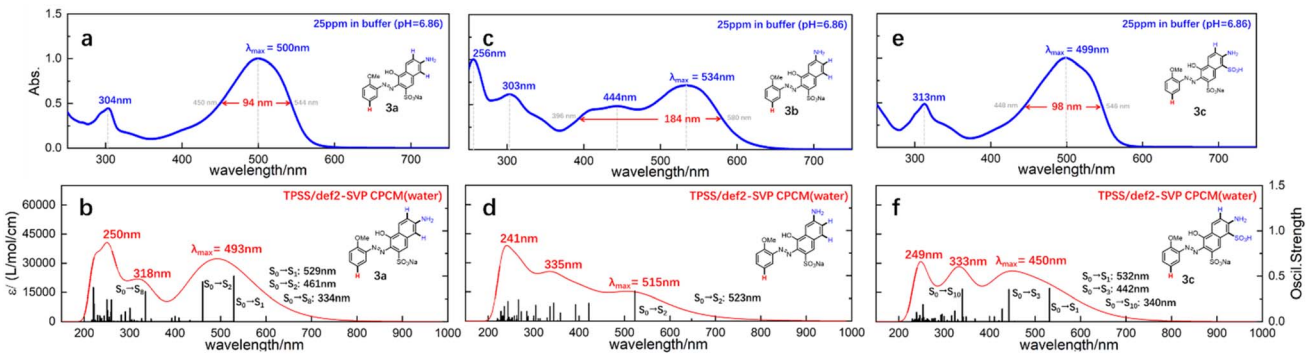

Fig. 2 Experimental (a), (c), (e) and theoretical (b), (d), (f) UV-Vis spectra of 3a–c.

atoms for **3a S1**, **3b S2**, and **3c S1**, and the shapes of **Hole**/**Ele** indicated those **ES** were mainly excited by a local π–π* transition. However, high-level ES made the absorption of **3b** different from that of **3a** and **3c**. For **3a S2** and **3c S3**, **Hole** was distributed on the naphthol ring and amino functional group, whereas the **Ele** appeared on the methoxyaniline. This process could be recognized as a charge transfer (**CT**) process in which electrons were excited from naphthol and transferred to parts of methoxyaniline. The 2,6-substituted (*para*-) positions of azo and amino groups kept the **Hole** and **Ele** far away to the greatest extent in **3a**/**3c**, which increased the dipole moment of **CT** and made the corresponding **OS** strong. The 2,7-substituted (*meta*-) positions of azo and amino groups in **3b** reduced the dipole moment of **CT** and made the excitation process of forming **S5** inefficient. A lot of low-efficiency high-energy **ES** were unneglectable and superimposed together, which elicited complexity to the excitation procedure and resulted in a broad absorption band in **3b**.

A fragment-divided study[14] was undertaken to investigate the contributions of naphthol (**Naph**), azo (**Azo**), and methoxyaniline (**Ph**) in the excitation process. As shown in Fig. 4, heatmaps using a white-to-black gradient ranging from 0% to 100% were applied to express the contributions of the fragments to **Hole** and **Ele**. Through this fragment-divided study, three detailed mechanisms could be postulated, as shown below.

(d) In most cases, **Naph** was the main contributor for **Hole** (*e.g.*, **S2**, **S3**, **S4** in **3a**, **S1**, **S3**, **S5**, **S6** in **3b**, and **S3**, **S4**, **S5**, **S6** in **3c**). HOMO–LUMO gap is equal to the energy level of HOMO minus the energy level of LUMO. And **Hole** is the region where electrons flow out, which can be treated approximately as LUMO. As a result, the increase of electronic density in **Hole** would narrowed energy gap by improving the energies of occupied orbitals, which may redshift λ_{max}. Besides, richer electronic density in **Hole** would prolong transition dipole moment and lead to the strengthening of corresponded **OS**, which facilitated the excitation process directly. To summarize, embedding EDG/EWG on **Naph** would shift λ_{max} to higher/lower value and strengthen/weaken the molar absorbance.

(e) **Azo** played the role as **Ele** in most cases, such as **S2**, **S3**, **S4**, **S5**, **S6** in **3a**, **S3**, **S4**, **S5**, **S6** in **3b**, and **S3**, **S4**, **S5**, **S6** in **3c**. However, in the cases of **S1** in **3a**, **S2** in **3b**, and **S1** in **3c** (which were the key **ES** contributing for λ_{max}), **Azo** acted as a **Hole**. As a result, increasing the electron density of **Azo** red-shifted the λ_{max} but blue-shifted other absorption bands, leading to broadening of the peak width. **Azo** was terminated by **Naph** and **Ph** at both ends, implying that the electron density of **Azo** was controlled by **Naph** and **Ph**. That is, the richer/poorer electron density on **Ph** or **Naph**, the richer/poorer electron density in **Azo**, resulting in greater/less λ_{max} and larger/smaller peak width.

(f) There was no significant tendency for **Ph** on the contribution of **Hole** or **Ele** during the excitation process. **Ph** acted as weak **Ele** where electrons flow into. However, in the cases of **S5** in **3a**, **S4** in **3b**, and **S6** in **3c**, **Ph** acted as strong donors for **Hole**. Consequently, the influence of functional groups with different electronegativities embedded on the benzene ring remained uncertain if inspection was done only on **Ph**.

Some additional experiments were carried out to verify the rationality of the inferences we made. Three azo products coupled with amidated J acids were prepared (Scheme 2, **4d–f**), and we conducted quantitative UV-Vis spectroscopy of **1–5a** and **4c**. The results for the molar absorption coefficient (ε), $W_{1/2}$, and λ_{max} are summarized in Scheme 2. As the electronegativity of the substituents embedded on **Ph** became stronger from **1a** to **5a**, the electron density in **Ph** decreased gradually, leading to the electron density declining in **Azo**. The descending of $W_{1/2}$ (**1a**,

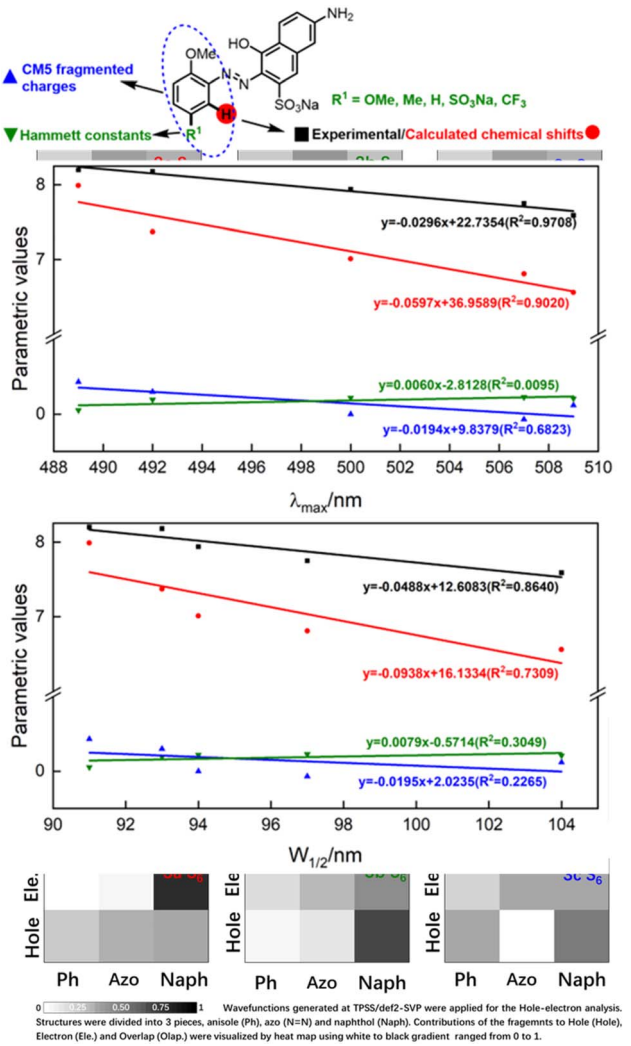

Fig. 4 Fragment analysis for Hole/Ele of 3a–c.

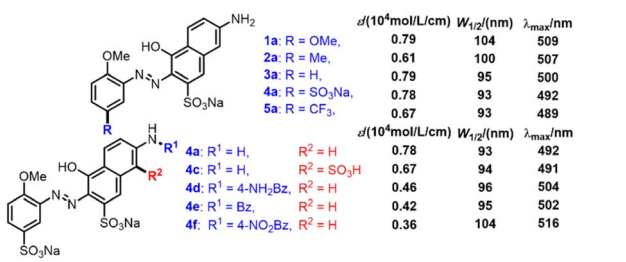

Scheme 2 ε, $W_{1/2}$, and λ_{max} of quantitative spectra.

104; **2a**, 100; **3a**, 95; **4a**, 93; **5a**, 93 nm) and λ_{max} (**1a**, 509; **2a**, 507; **3a**, 500; **4a**, 492; **5a**, 489 nm) from **1a** to **5a** verified the correctness of inference (e). Conversely, in the series of **4a** and **4d–f**, with the decoration of benzoyl functional groups on amino groups, the electron density of **Naph** fell gradually. The change in ε provided direct evidence of the decrease in **OS** (**4a**, 0.78; **4d**, 0.46; **4e**, 0.42; **4f**, 0.36), which was consistent with inference (d) that EWG embedded on **Naph** led to **OS** weakening. The slight drop in ε, and the high consistency of $W_{1/2}$ and λ_{max} of **4a** and **4c** revealed the poor electron-withdrawing effect of the sulfonic-acid group connected to **Naph**, which had little influence on the electron density and spectral properties of **Naph**. All these supplementary experiments supported the conclusions made by hole–electron analysis overall, and verified the key roles of electronegativity in spectral features.

Quantitative predictions of UV-Vis spectra

Having qualitatively established the relationship of structure and spectral features, some further works focusing on quantitative predictions of UV-Vis spectra were conducted. As described in inferences (e) and (f), a functional group with different electronegativity embedded on the benzene ring would tune the electron density of azo groups, and influence the UV-Vis spectra. However, quantitative predictions of UV-Vis spectra relied on a robust parametric method to depict the electronegativity of functional groups, which was beyond the scope of the hole–electron analysis.

The electron density was the key point of quantitative predictions of UV-Vis spectra, so long-tested Hammett constants[15] and CM5 charge populations of the fragments[16] were selected as parametric methods. In addition, the NMR shift had been widely applied for characterizing functional-group electronegativity so that EWG shifted the signals to a high field and EDG shifted the signals to a low field. Hence, experimental chemical shifts and calculated chemical shifts[17] were also taken into consideration (more details in Fig. S3, S4, and Scheme S3†).

As shown in Fig. 5, λ_{max} and $W_{1/2}$ were set as *x*-axes and parametric values were set as *y*-axes. Comparison of R^2 values revealed that the experimental chemical shifts had the best linearity to λ_{max} and $W_{1/2}$ (R^2 = 0.9708 and 0.8640), and the calculated chemical shifts (R^2 = 0.9020 and 0.7390) were slightly inferior to the experimental ones. However, Hammett constants and CM5 fragmented charges performed far worse than NMR spectroscopy did. We believe the poor performances of Hammett constants and CM5 fragmented charges were due to the nonlinear relationship between functional-group electronegativity and electron densities of **Ph**. Also, the chemical shifts obtained by NMR spectroscopy were more closely associated with the electron densities of **Ph**. As a result, the chemical shifts obtained by NMR spectroscopy performed better in describing the electron densities of aromatic rings and reproducing the influences of the electron effect on UV spectra more precisely.

To conclude, λ_{max} and $W_{1/2}$ could be described by the experimental chemical shifts (ECS)/calculated chemical shifts (CCS) using the following formula:

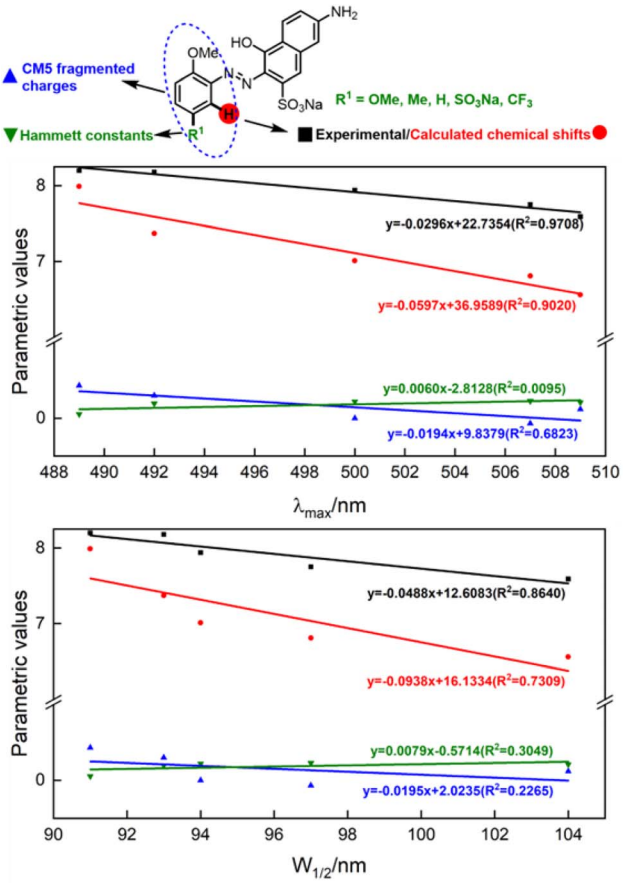

Fig. 5 Linear fitting of λ_{max} and $W_{1/2}$ of **1–5a**.

$$ECS = -0.0296\lambda_{max} + 22.7354\ (R^2 = 0.9708) \quad (a)$$

$$CCS = -0.0597\lambda_{max} + 36.9589\ (R^2 = 0.9020) \quad (b)$$

$$ECS = -0.0488 W_{1/2} + 12.6083\ (R^2 = 0.8640) \quad (c)$$

$$CCS = -0.0938 W_{1/2} + 16.1334\ (R^2 = 0.7309) \quad (d)$$

Regardless of the inferior accuracies, the easy acquisitions of CCS with no need for synthetic operations or expensive equipment would greatly promote construction of a library of spectral parameters. We believe the accuracy would lead to further improvements with the development of better methods for theoretical NMR calculation, which would be of great benefit to the systematic study of azo compounds.

Some compounds (**6a–9a**) were prepared to verify the applicability of the fitted formulas. The experimental/predictive λ_{max} and $W_{1/2}$ of some extra-prepared monoazonaphthols were summarized (Scheme 3). The predictions for **6a** and **7a** had relative high accuracy; the predicted $\lambda_{max}/W_{1/2}$ matched with the experimental one with an error of less than 3%/7%. However, the prediction of **8a** and **9a** had poor precision; λ_{max} and $W_{1/2}$ were overestimated. Referring to experimental NMR spectra, we found the experimental chemical shifts of **8a** and **9a** to be 7.79 ppm and 7.59 ppm, respectively, and deviated from the calculated ones (7.01 ppm and 6.92 ppm, respectively).

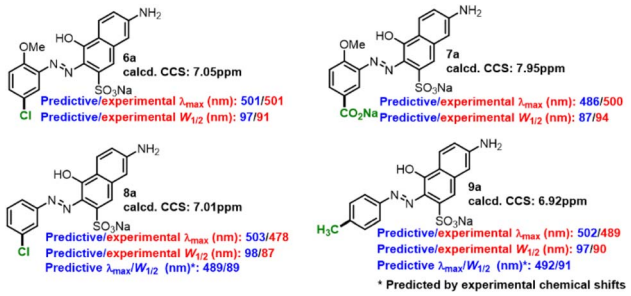

Scheme 3 Predictive and experimental λ_{max} and $W_{1/2}$ of **6a–9a**.

Replacing the calculated chemical shifts with the experimental ones revealed that the errors of the predicted λ_{max} and $W_{1/2}$ of **8a** and **9a** decreased obviously. Therefore, we believe that the constructed linear prediction model could act in more general situations if a precise method of NMR calculation was developed. Predicted λ_{max} and $W_{1/2}$ of other *o*-methoxyaniline-terminated azo dyes were calculated (more details in ESI†), which laid the foundation for the construction of spectral libraries.

Conclusions

Twenty-two new types of monoazonaphthols were synthesized, and UV-Vis absorption spectra collected. Detailed DFT/TD-DFT calculations were also conducted to elicit in-depth understanding of excitation mechanism. The combined experimental and DFT study revealed excitation details and excitation mechanisms about the formation of UV-Vis spectra, and rationally explained how chemical structures influenced transition dipole moments, excitation behaviours, and spectra features. Fragmented-divided hole–electron analyses revealed the contributions of different fragments to the excitations process, and that naphthol parts provided electrons to transfer into azo N=N double bonds. These findings qualitatively revealed why EDG/EWG decorated naphthol shifted absorption wavelengths to higher/lower values and strengthened/weakened molar absorbance, whereas azo N=N double bonds with embedded EDG/EWG resulted in greater/less λ_{max} and larger/smaller peak widths. Moreover, a linear model connecting the λ_{max} and $W_{1/2}$ to NMR chemical shifts was constructed, which showed good accuracies (error < 7%) in the prediction of λ_{max} and $W_{1/2}$ of *o*-methoxyaniline-terminated monoazonaphthol. This linear model could be expanded to the prediction of UV-Vis spectra of other aniline-terminated monoazonaphthols with little loss in accuracy. A library of larger compounds and more theoretical NMR calculation methods are under study. We believe this work could pave the way for deeper understanding of the UV-Vis spectra of azo compounds, and bring new insights for parametric description of UV-Vis libraries.

Conflicts of interest

There are no conflicts of interest to declare.

Acknowledgements

This work was supported by the Special Fund Projects of Guangdong Academy of Sciences for the Construction of Domestic First-class Research Institutions (2021GDASYL-20210103035).

Notes and references

1 A. Bafana, S. S. Devi and T. Chakrabarti, *Environ. Rev.*, 2011, **19**, 350–370.
2 R. B. Chavan, *Handbook of Textile and Industrial Dyeing (in Woodhead Publishing Series in Textiles). Principles, Processes and Types of Dyes*, 2011, vol. 1, pp. 515–561.
3 For selected papers on spectra studies and dyes designing, see:(*a*) S. Benkhaya, S. M' rabet and A. El Harfi, *Inorg. Chem. Commun.*, 2020, **115**, 107891; (*b*) H. A. Shindy, *Dyes Pigm.*, 2017, **145**, 505–513; (*c*) S. Shahab, F. H. Hajikolaee, L. Filippovich, M. Darroudi, V. A. Loiko, R. Kumar and M. Y. Borzehandani, *Dyes Pigm.*, 2016, **129**, 9–17.
4 For selected patents or papers on redshift or blueshift control of dyes, see: (*a*) G. Zhu, J. Jiang, Z. Li, H. Song and Y. Zeng, 2022, CN114539803A; (*b*) B. Chen, S. Ni, L. Sun, X. Luo, Q. Zhang, Y. Song, Q. Zhong, Y. Fang, C. Huang, S. Chen and W. Wu, *Dyes Pigm.*, 2018, **158**, 474–481.
5 For selected papers on recent applications of dyes, see: (*a*) J. Gong, K. Sumathy, Q. Qiao and Z. Zhou, *Renewable Sustainable Energy Rev.*, 2017, **68**, 234–246; (*b*) G. Richhariya, A. Kumar, P. Tekasakul and B. Gupta, *Renewable Sustainable Energy Rev.*, 2017, **69**, 705–718; (*c*) K.-H. Kim, S. Lee, C.-K. Moon, S.-Y. Kim, Y.-S. Park, J.-H. Lee, J. W. Lee, J. Huh, Y. You and J.-J. Kim, *Nat. Comm.*, 2014, **5**, 4769; (*d*) J. B. Chang, J. H. Hwang, J. S. Park and J. P. Kim, *Dyes Pigm.*, 2011, **88**(3), 366–371; (*e*) N. Mochizuki, T. Ishinabe, D. Fujiwara, D. Nakamura, N. Koma and H. Fujikake, *ITE Trans. Media Technol. Appl.*, 2018, **6**(4), 262–268; (*f*) K. Nobuhiro and F. Keita, *Chem. Lett.*, 2005, **34**, 558–559.
6 Reviews on the developments of TD-DFT studies, see: (*a*) A. D. Laurent, C. Adamo and D. Jacquemin, *Phys. Chem. Chem. Phys.*, 2014, **15**, 14334–14356; (*b*) A. D. Laurent and D. J. Jacquemin, *J. Quantum Chem.*, 2013, **113**(17), 2019–2039; (*c*) A. Drzewiecka-Matuszek and D. Rutkowska-Zbik, *Molecules*, 2021, **26**(23), 7176.
7 For selected papers on recent developments of analytical methods for TD-DFT calculations, see: (*a*) M. Nakano, H. Fukui, T. Minami, K. Yoneda, Y. Shigeta, R. Kishi, B. Champagne, E. Botek, T. Kubo, K. Ohta and K. Kamada, *Theor. Chem. Acc.*, 2011, **130**, 711–724; (*b*) M. Campetella, F. Maschietto, M. J. Frisch, G. Scalmani, I. Ciofini and C. Adamo, *J. Comput. Chem.*, 2017, **38**, 2151–2156; (*c*) T. L. Bahers, C. Adamo and I. Ciofini, *J. Chem. Theory Comput.*, 2011, **7**, 2498–2506; (*d*) Z. Liu, T. Lu and Q. Chen, *Carbon*, 2020, **165**, 461–467.
8 Reported methods about diazotization control, see: (*a*) W. Chen, P. Gao, H. Jiang and Z. Cui, *Dyes Pigm.*, 2019,

168, 300–310; (*b*) Q. Guo, W. Chen, P. Gao, J. Zheng, H. Jiang and Z. Cui, *Dyes Pigm.*, 2022, **204**, 110469.

9 Software and program involved in this paper, see: (*a*) F. Neese, *Wiley Interdiscip. Rev.: Comput. Mol. Sci.*, 2012, **2**, 73–78; (*b*) F. Neese, *Wiley Interdiscip. Rev.: Comput. Mol. Sci.*, 2018, **8**, e1372; (*c*) F. Neese, F. Wennmohs, U. Becker and C. Riplinger, *J. Chem. Phys.*, 2020, **152**, 224108; (*d*) F. Neese, *Wiley Interdiscip. Rev.: Comput. Mol. Sci.*, 2022, **12**(5), e1606; (*e*) N. M. O'Boyle, M. Banck, C. A. James, C. Morley, T. Vandermeersch and G. R. Hutchison, *J. Cheminf.*, 2011, **3**, 33; (*f*) T. Lu and Q. Chen, *Comput. Theor. Chem.*, 2021, **1200**, 113249; (*g*) T. Lu and F. Chen, *J. Comput. Chem.*, 2012, **33**, 580–592; (*h*) E. D. Glendening, C. R. Landis and F. Weinhold, *J. Comput. Chem.*, 2019, **40**, 2234–2241; (*i*) E. R. Alan and W. J. Frank, *Chem. Phys.*, 1983, **78**, 4066–4073.

10 T. A. Halgren, *J. Comput. Chem.*, 1996, **17**, 490–519.

11 Methods applied in DFT calculations, see: (*a*) A. D. Becke, *J. Chem. Phys.*, 1993, **98**, 5648–5652; (*b*) C. Lee, W. Yang and R. G. Parr, *Phys. Rev. B: Condens. Matter Mater. Phys.*, 1988, **37**, 785–789; (*c*) B. Miehlich, A. Savin, H. Stoll and H. Preuss, *Chem. Phys. Lett.*, 1989, **157**, 200–206; (*d*) F. Weigend and R. Ahlrichs, *Phys. Chem. Chem. Phys.*, 2005, **7**, 3297–3305; (*e*) S. Grimme, J. Antony, S. Ehrlich and H. Krieg, *J. Chem. Phys.*, 2010, **132**, 154104; (*f*) S. Grimme, S. S. Ehrlich and L. Goerigk, *J. Comput. Chem.*, 2011, **32**, 1456–1465; (*g*) V. Barone and M. Cossi, *J. Phys. Chem. A*, 1998, **102**, 1995; (*h*) J. Tao, J. P. Perdew, V. N. Staroverov and G. E. Scuseria, *Phys. Rev. Lett.*, 2003, **91**, 146401.

12 G. Zhu, Z. Chen, H. Song, A. You and Z. Li, *RSC Adv.*, 2022, **12**, 18238.

13 M. J. Hollas, *Modern Spectroscopy*, Wiley, 3rd edn, 1996, pp. 30–34.

14 Recent papers applying Hole-Electron analysis disclosing excitation features, see: (*a*) S. Chen, N. Ullah and R. Zhang, *J. Phys. Chem. Lett.*, 2018, **9**, 4857; (*b*) X. Tang, L.-S. Cui, H.-C. Li, A. J. Gillett, F. Auras, Y.-K. Qu, C. Zhong, S. Jones, Z.-Q. Jiang, R. H. Friend and L.-S. Liao, *Nat. Mater.*, 2020, **19**, 1332; (*c*) X. Wang, Z. Liu, X. Yan, T. Lu, H. Wang, W. Xiong and M. Zhao, *Phys. Chem. Chem. Phys.*, 2022, **24**, 7466.

15 C. Hansch, A. Leo and R. W. Taft, *Chem. Rev.*, 1991, **91**(2), 165–195.

16 A. V. Marenich, S. V. Jerome, C. J. Cramer and D. G. Truhlar, *J. Chem. Theory Comput.*, 2012, **8**(2), 527–541.

17 M. T. Oliveira, J. M. A. Alves, A. A. C. Braga, D. J. D. Wilson and C. A. Barboza, *J. Chem. Theory Comput.*, 2021, **17**(11), 6876–6885.